International Journal of Impact Engineering 62 (2013) 13–26

Contents lists available at SciVerse ScienceDirect

International Journal of Impact Engineering

journal homepage: www.elsevier.com/locate/ijimpeng

In situ diagnostics for a small-bore hypervelocity impact facility

J.M. Mihaly*, J.D. Tandy, M.A. Adams, A.J. Rosakis

California Institute of Technology, MC 205-45, 1200 E. California Blvd, MC 105-50, Pasadena, CA 91101, United States

ARTICLE INFO

Article history:
Received 30 January 2013
Received in revised form
23 April 2013
Accepted 21 May 2013
Available online 31 May 2013

Keywords:
Hypervelocity impact
High-speed imaging
Debris capture
IR emission
Spectroscopy

ABSTRACT

New *in situ* diagnostic capabilities and improvements made to the previously reported 1.8 mm bore, two-stage light-gas gun facility located at the California Institute of Technology are described. The Small Particle Hypervelocity Impact Range (SPHIR) facility is capable of routinely producing launch speeds of 5–7 km/s for launch package masses < 6 mg, with maximum speeds exceeding 10 km/s. The facility features a comprehensive ensemble of *in situ* diagnostics that are available for simultaneous implementation in every impact experiment. A fast (150,000 fps) camera is used routinely to provide impactor velocimetry. A gated, intensified ultra-high-speed camera is used in conjunction with an optical technique to create shadowgraph images of hypervelocity impact phenomena with very short exposure times (25 ns) and inter-frame times (<1 μs). This technique uses a constant 532 nm wavelength laser to deliver a collimated, coherent illumination beam orthogonal to the projectile flight direction that provides a 100 mm diameter maximum field of view. The ultra-high-speed camera produces 8 images with exposure and inter-frame times sufficiently short to enable sharp visualization of impact features with little motion blur at the test speeds of 5–7 km/s. Additionally, a debris capture system is located behind the target configuration during every experiment. This system is composed of layers of closed-cell foam and plastic film and provides depth of penetration and trajectory measurement for debris particles thrown behind the target. Lastly, the SPHIR facility utilizes two additional high-speed cameras coupled with two spectrographs to characterize the light emitted by the impact event. One spectrograph and its high-speed camera records UV–visible emission spectra in the wavelength range between 300 nm and 850 nm. The other spectrograph uses a high-speed, infrared camera to capture a single full-field image of the near-IR emission in the wavelength range of 0.9 μm–1.7 μm. These two spectrograph camera systems provide both visual and spectral data of the hypervelocity impact emission; yielding information regarding the molecular composition of both the impact ejecta and debris. The extensive diagnostic capabilities and techniques described can be used with a wide variety of impactors, target materials and target configurations to address a wide variety of engineering and scientific problems.

1. Introduction

Hypervelocity impact of meteoroids and orbital debris (MOD) on spacecraft poses a serious threat to spacecraft survival. Any spacecraft, particularly those intended for long duration spaceflight or entry, descent, and landing (EDL) must be designed with the capability to withstand extended exposure to the MOD environment. The Columbia accident serves as a tragic reminder of the critical nature of an entry vehicle's heat shield health and the potentially catastrophic consequences [1] of significant impact damage. Furthermore, the severity of the orbital debris environment continues to grow at an increasing rate as international involvement in space increases. Therefore, the importance of MOD shielding on spacecraft, and the continued improvement of shielding systems, is of paramount importance as the aerospace industry develops its next generation of space exploration vehicles.

Hypervelocity impacts induce a complex dynamic material response, which includes numerous interacting phenomena such as mixed phase flow, fragmentation, spallation, melting, vaporization, and ionization [2]. Due to such complexity, modeling success has been limited and remains inadequate. The current understanding of hypervelocity impact damage is obtained largely through experimental evaluation [3,4] of MOD shielding systems. The empirical models used to describe this data are specific to the materials/component configurations used in the tests and the test conditions. Such models cannot be safely extrapolated to other materials or conditions. Furthermore, given the high operating cost

* Corresponding author. Tel.: +1 6263954514.
E-mail address: jmmihaly@caltech.edu (J.M. Mihaly).

0734-743X/$ – see front matter © 2013 Published by Elsevier Ltd.
http://dx.doi.org/10.1016/j.ijimpeng.2013.05.004

Abbreviations

AGS	Average Grayscale
LSL	Laser Side-Lighting
MOD	meteoroids and orbital debris
SPHIR	Small Particle Hypervelocity Impact Range

of many impact facilities, the extensive shield testing required to adequately characterize the variability and hence, the uncertainty in shield performance can be prohibitively expensive. Often inadequate data exists to describe the stochastic damage mechanics that govern shield system performance. Therefore, the aerospace industry would greatly benefit from the development and implementation of low-cost methods to help characterize hypervelocity impact phenomena.

2. Facility overview

The Graduate Aeronautical Laboratories at the California Institute of Technology (GALCIT) has established the Small Particle Hypervelocity Impact Range (SPHIR), shown in Fig. 1, an experimental facility designed to study MOD impacts [5]. The facility's two-stage light-gas gun [6] uses compressed hydrogen or helium gas to launch small particles with diameters of 1.8 mm, to velocities up to 10 km/s. These launch packages are accelerated downrange into a large (1 m × 1 m × 2 m) target chamber with atmospheric levels maintained at pressures ranging between 1 and 50 mmHg (0.13–6.67 kPa). Launch packages are accelerated in a disposable, smooth bore (non-rifled) launch tube, which helps reduce the operational cost of the facility but makes the use of sabots more difficult.

The masses launched and the velocities attained in this facility are a good analog for MOD studies, but are not particularly unique. However, the SPHIR facility is unique given the array of simultaneous high-speed optical diagnostics operating routinely on each experiment. The facility therefore combines a low-cost of operation with high-volume of data output from each experiment. The large target chamber features multiple view-ports enabling the simultaneous observation of the experiment with a suite of high-speed diagnostics (described herein). The target chamber is shown in Fig. 2.

2.1. Impactor velocimetry

A common method to measure the impactor speed in light-gas gun experiments is to use a series of laser barriers which are interrupted by the impactor during its flight to the target. However, several factors complicate the application of such a method in the SPHIR facility. First, a luminous cloud of high temperature hydrogen gas precedes the exit of the impactor from the launch tube and follows the impactor in its flight to the target. Additionally, the small bore (1.8 mm) of the SPHIR facility requires the use of impactors that are smaller than those utilized in many other light-gas gun facilities. As a consequence, the detector signal interruption produced by the passing of such a small impactor at hypervelocities is brief and obscured by a low signal-to-noise ratio. These factors would therefore require the implementation of a specialized optical system [7] to utilize the laser barrier technique.

A simpler, less complex, solution is to use the Photron SA1 Fastcam to measure the impactor speed. When the impactor is traveling at greater than 4 km/s, the low-pressure atmosphere (0.13–6.67 kPa) in the evacuated target chamber is ionized directly

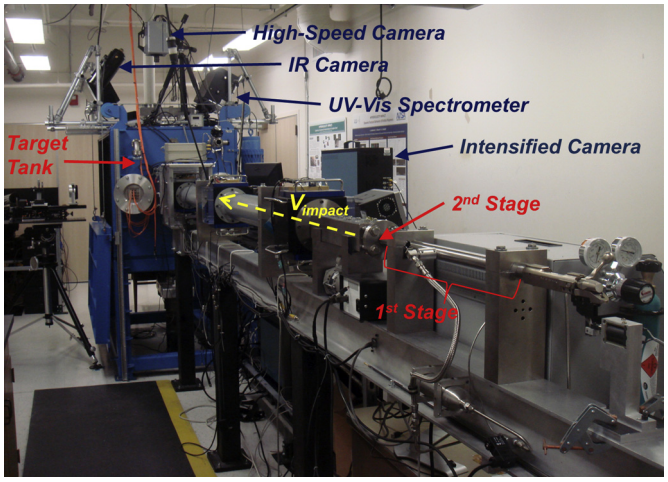

Fig. 1. The Small Particle Hypervelocity Impact Range (SPHIR) facility at Caltech. Diagnostics have been developed and implemented to complement this two-stage light-gas gun facility.

in front of the impactor and forms a luminescent sheath surrounding and trailing the location of the impactor. This hot plasma sheath radiates sufficient light to enable high-speed imaging by self-illumination.

As shown in Fig. 1, the Photron camera is mounted above the target chamber looking down upon the flight path of the impactor. The distance from the camera to the impactor velocity vector is approximately fixed at 1.2 m with respect to the camera. A 25 mm, f/0.95 lens is configured with the Photron camera and provides a field of view of approximately 160 mm × 94 mm. The lowest available relative aperture is used to collect the maximum amount of light radiated by the impactor. At the nominal operating framing rate of 150,000 fps, this field of view is observed with 192 × 112 pixel resolution. A mirror, angled toward the target, is also located at the bottom of the target tank within the Photron camera's field of view. An illustration of this setup is provided by Fig. 3. This configuration allows visualization of both the impactor in flight to the target and the subsequent target impact flash. An

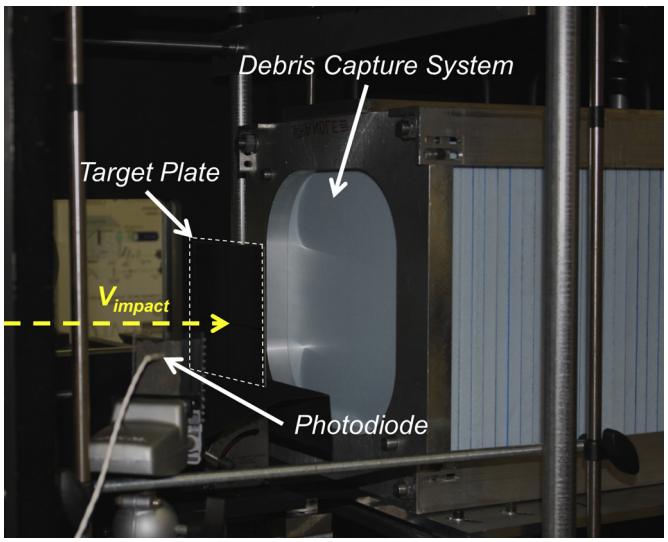

Fig. 2. Target chamber of the SPHIR facility, with target plate and nominal impactor velocity vector identified. The photodiode used to trigger diagnostics and the debris capture system is also shown.

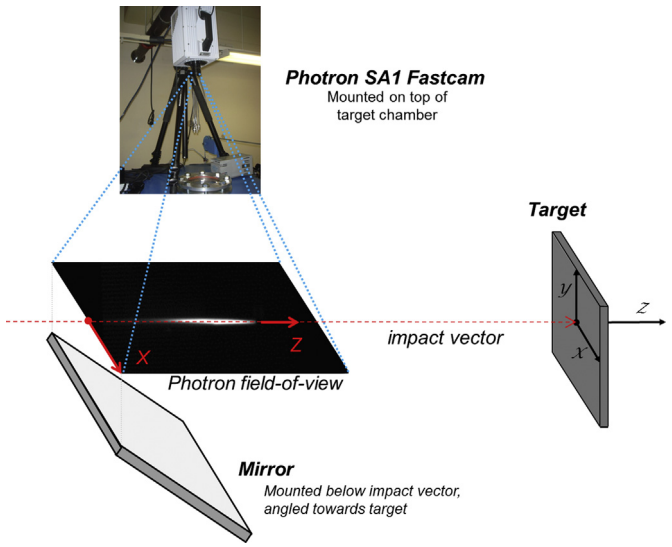

Fig. 3. The Photron fast camera configuration used to measure the impact velocity.

example of images taken by the Photron fast camera is provided in Fig. 4 below. The series of images presented depict the impactor visible as a "shooting star" passing below the camera before becoming visible again later as a reflection in a mirror when impact on the target occurs in frame n_0. With these images, the position of the impactor can be accurately determined at several positions at precise times.

The impactor speed can then be computed from a single frame by considering the distance of the impactor from the target and the corresponding time of flight to the target. The field of view of the Photron camera is calibrated such that the distance to the target of each pixel is known. For example, considering Fig. 4, the distance to the target is known from the shock-front observed in frame $n = -\mathrm{i}$. The time of flight is then measured given the number of frames until the impact is observed in frame $n = 0$. With the distance traveled and time of flight known, the velocity of the impactor can then be estimated.

However, this method is limited by the uncertainty in the time of flight. At Photron framing rates of 150,000 fps this corresponds to upwards of 6.67 μs, which can represent greater than 5% of the total time of flight. Including the uncertainty in the measured distance to target, the corresponding uncertainty for this method would be ±7% or more for velocity measurements between 5 and 7 km/s. A more accurate alternative is to measure the relative position of the impactor in sequential images taken with the Photron camera. The inter-frame timing of the Photron camera is very precise; therefore the accuracy of tracking the impactor is dominated by the definition of the impactor position.

2.1.1. Definition of impactor position

This plasma sheath surrounding and trailing the impactor is visible in the Photron camera as a coma, or illuminated streak of

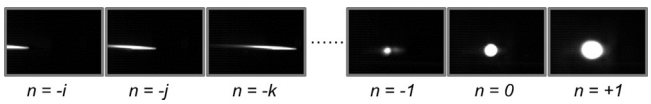

Fig. 4. Sequence of images from the Photron fast camera used to measure the velocity of a 1.8 mm diameter nylon right cylinder. The camera recorded this sequence at 150,000 fps. The three images on the left (frames −i, −j, −k) depict the self-illuminating impactor moving from left to right through the camera's field of view. The three images on the right visualize the target impact as a reflection in a mirror. Impact occurs in frame $n = 0$. The impactor is visible immediately before impacting the target in frame $n = -1$.

excited gas particles. Assuming the plasma sheath surrounding the impactor is non-reactive, the shock-front is the brightest point in the plume. Therefore, the position of the impactor, as measured through the camera, is related to the shock-front position of the tumbling impactor [8].

The observed position of the shock-front is measured by considering the grayscale values recorded on the camera CCD by the observed coma. The coordinate system used in considering the CCD data is presented in Fig. 3. The longitudinal Z-direction is defined as an axis collinear with the velocity vector of the impactor. Subsequently, the vertical axis in the Photron camera's image is parallel to the target in-plane x-direction. The origin used in the velocimetry analysis is the point on the left (uprange) edge of the CCD along the impactor velocity vector.

The grayscale of the coma is plotted in the longitudinal Z-direction (along the impactor velocity vector). Given the current default length-scale of the Photron's field of view (0.83 mm/pixel), the entirety of the (original) impactor can be resolved with three pixels. Therefore, an analysis of the observed coma is performed by considering the grayscale profiles along three lines of constant X. The three X-coordinates are determined by first locating the X-coordinate with the highest cumulative grayscale and then identifying the two adjacent X-coordinates. The average of the grayscale of these three X-coordinates at each longitudinal (Z) position is computed to produce an Average Grayscale (AGS) curve for each of the images recorded in a sequence. The "peak brightness" of each observed coma is then quantified as the maximum of each AGS curve. An example of a sequence of AGS curves is presented in Fig. 5.

To reduce errors associated with the determination of the coma's leading edge and help define the uncertainty in the measurement, the leading edge is defined using three methods. The first method is to locate the forward-most pixel with a grayscale level higher than a defined threshold. This threshold is prescribed to distinguish the coma from the image's background grayscale (noise).

However, depending on the brightness of the shock-front and the sensitivity of the Photron CCD, the leading edge of the coma measured for each Photron image does not necessarily correspond to the physical location of the impactor's shock-front. This is a consequence of the impactor moving while the image is observed. The default exposure time used in the operation of the Photron camera is 6.67 μs, which corresponds to the nominal framing rate of 150,000 fps. Therefore, at 6 km/s the impactor would traverse 40 mm across the camera's field of view. Consequently, the brightness (i.e. grayscale) measured on each individual pixel of the Photron CCD is the cumulative illumination recorded during this entire exposure time.

The standoff distance of the shock-front with respect to the centroid of the impactor is approximately constant, independent of tumbling [8]. Therefore, when the amplitude of the observed coma brightness is similar, the relative physical position of the impactor with respect to the observed coma remains constant. Accordingly, a comparison of sequential frames would provide an accurate measurement of the impactor speed, regardless of any uncertainty between the observed coma and relative physical impactor position. The peak brightness of the recorded comas has been observed to vary by small amounts between sequential frames. A cylinder with a nonzero angle of attack would lead to brighter self-illumination compared to a cylinder with zero degree angle of attack. Because the response of the CCD is approximately uniform with respect to a constant illumination source, the observable disparity in coma brightness is likely a consequence of impactor tumbling.

The two additional methods used to define the coma leading edge compensate for disparities in the observed coma brightness

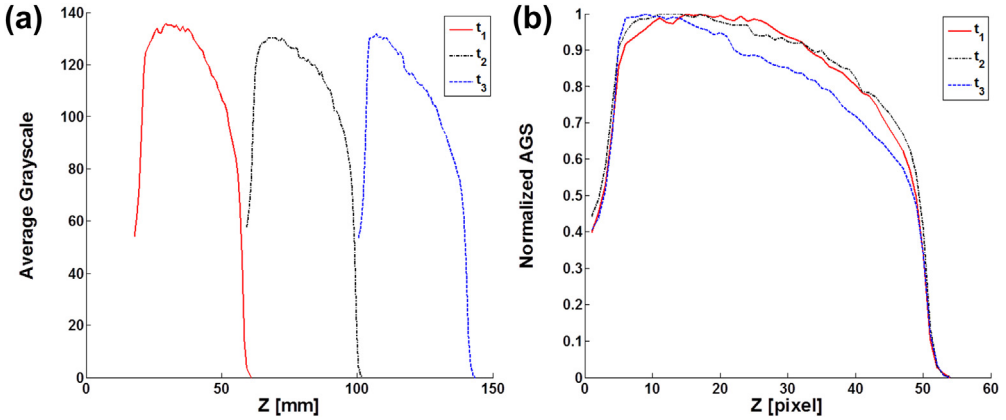

Fig. 5. (a) Example of Average Grayscale (AGS) profile curves from subsequent images recorded by the Photron fast camera. Each AGS curve is obtained by averaging the three brightest grayscale profiles in the Z-direction. (b) Normalized AGS curves plotted together to illustrate structural similarity.

between frames by normalizing each AGS curve with respect to its peak brightness. Normalization is used to preserve the characteristic structure of each of the AGS curves. If the curves are characteristically the same shape, it is reasonable to conclude that the physical process creating the observed curves, and therefore defining the relative position of the impactor, is self-similar. Fig. 5 provides an example of normalized curves plotted together for the purpose of demonstrating similarities in the structure of AGS curve during a sequence of high-speed images. The second method to determine the coma leading edge defines the leading edge as a constant value on the normalized AGS curve (typically between 0.2 and 0.4). The third and final technique considers the gradient of each normalized AGS curve and defines the leading edge as the steepest point on the (forward-most) rising-edge common to each of the curves.

2.1.2. Velocity measurement and uncertainty

The location of the shock-front leading edge is defined, as described, using three different methods. For each leading edge definition, the impactor speed is then computed using Eq. (1). The positions of the leading edge in the first and last image of the sequence recorded by the Photron camera are considered to maximize the distance and time quantities and subsequently reduce measurement uncertainty. Results for impactor speeds using each of the three leading edge definitions are similar. The reported speed is then taken as the average of the speeds computed using the three leading edge definitions.

The uncertainty of the impactor speed measurement Eq. (2) is then quantified by considering the root-sum-square (RSS) of the independent error contributions from measurements of pixel distances (Δp), time (Δt), and pixel length-scale (S) used to compute the impactor speed.

$$v = \frac{S\Delta p}{\Delta t} \tag{1}$$

$$\varepsilon_v = \sqrt{\left(\frac{\partial v}{\partial \Delta p}\varepsilon_{\Delta p}\right)^2 + \left(\frac{\partial v}{\partial \Delta t}\varepsilon_{\Delta t}\right)^2 + \left(\frac{\partial v}{\partial S}\varepsilon_S\right)^2} \tag{2}$$

Comparison of the three leading edge definitions provides an independent an estimate in the uncertainty in inter-frame pixel distance (ε_p): nominally only 1 pixel. The uncertainty of the timing of the Photron camera is less than 100 ns. Based on disparities in consecutive calibrations, the uncertainty of the Photron camera's field of view is estimated as 8.3×10^{-3} mm/pixel. Given the distance of the camera from the impactor velocity vector, a misalignment of the camera of 5 degrees with respect to vertical would correspond to only a 0.4% disparity in the observed field of view length. The corresponding effect on the camera pixel length-scale and uncertainty would therefore be minimal. With the described parameter uncertainties, a conservative estimate of the impact speed measurement uncertainty is nominally ±1.5%. Therefore, for a measured impact speed of 6000 m/s, the corresponding uncertainty is typically 90 m/s. The disparity between the velocities computed using the three leading edge definitions is within the uncertainty of the measurements and nominally less than 1% of the total velocity.

2.2. Facility performance

The 1.8 mm diameter, $L/D = 1$ Nylon 6/6 cylinders have an average mass of 5.5 mg. Using hydrogen as the light-gas, typical impact speeds range from 5 to 7 km/s, with a mean of 5.7 km/s and a median of 5.6 km/s Fig. 6 reports the performance (as a cumulative distribution function) of the SPHIR facility launching 5.5 mg

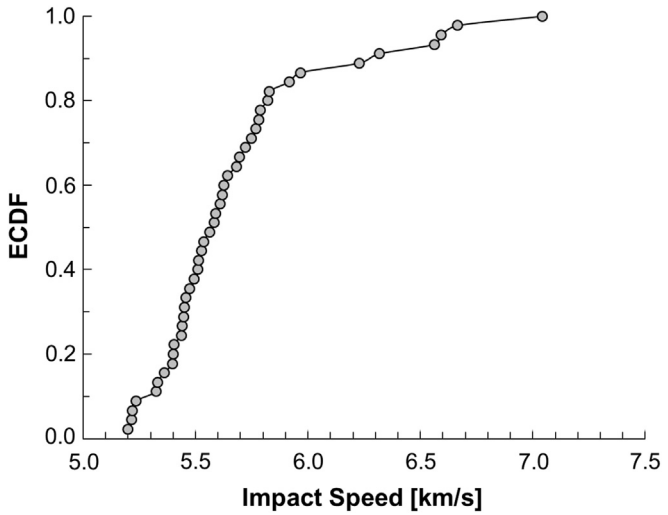

Fig. 6. Empirical cumulative distribution function (ECDF) reporting the impact speed performance of the SPHIR facility for 5.5 mg Nylon 6/6 cylinders launched into 1–2 mmHg of atmospheric pressure using 150 psi of compressed H_2.

Nylon 6/6 impactors into 1–2 mmHg (133–266 Pa) of atmospheric pressure using 150 psi of compressed H_2. The CDF is determined through median ranked statistics for 45 experiments, assuming equal probability of each observed result. Furthermore, the cylinder impactors have been observed to tumble with high angular velocities (as expected) estimated as at least 250,000 rpm.

2.3. Triggering

An impact flash observing detector, as previously presented in Fig. 2, is used to provide the triggering signal for all of the simultaneously operated high-speed diagnostics utilized in the SPHIR facility. The trigger circuit features an LED photodiode positioned approximately 20 cm from the target to observe the impact flash produced during an experiment. The spectral bandwidth range of the photodiode is from 620 to 980 nm. Upon flash detection, the trigger circuit outputs a 5 V DC signal to two Berkley Nucleonics Corporation (BNC) Model 575 pulse generators. The two pulse generators output 5 V TTL (transistor–transistor logic) trigger signals to all instruments and data acquisition systems with less than 170 ns total delay and 20 ps jitter. Given that all instruments are operated using the same trigger signal, the relative timing between instrument measurements is then very precisely known (to within 10 ns).

With a very low number of trigger failures (much less than 1% of all experiments), this triggering method has proven to be very robust. However, there is a finite delay between the actual impact and triggering of the instrumentation. This delay corresponds to the formation of the impact flash, detection of the flash's growing luminosity, and response time of the phototransistor. Therefore, the physical time t of an instrument's measurement is given by Eq. (3), where t_{trig} is the finite delay between impact and subsequent generation of the triggering signal. The instrument delay time t_{del} and frame exposure (shutter) time t_{exp} are programmed for each instrument and monitored with high precision using 2.5 GS/s, 1 GHz oscilloscopes. Analysis of the debris cloud and backward extrapolation of the debris front (described in Section 5) can provide an estimate for the length of the triggering delay. Nominal trigger signal response times after impact are approximately 1 microsecond (for 1 mmHg target chamber pressure).

$$t = t_{trig} + t_{del} + t_{exp} \tag{3}$$

3. *In situ* high-speed optical diagnostics

3.1. Laser Side-Lighting (LSL) ultra-high-speed photography

An optical technique has been developed to create shadowgraph images of hypervelocity impact events with very short exposure times (25 ns) and short inter-frame times (<1 μs). This short exposure time enables sharp visualization of impact features with very little motion blur at the test speeds of 5–7 km/s. This technique uses illumination orthogonal to the projectile flight direction to provide a shadowgraph image of the impact on the target with a perspective similar to those produced by Piekutowski [9,10]. The distinguishing feature of this optical imaging system is the use of a collimated, constant wave coherent light source.

Historically, flash X-ray systems have been used [9–11] to observe and analyze the evolution of debris clouds. High-speed photography has also provided an alternative to the imaging of hypervelocity impact debris formation [12]. Advances in modern digital photography have improved both the quality and utility of high-speed photography as a method to study debris phenomena in hypervelocity impact experiments [13,14]. Many digital photography systems [15] commonly utilize flash lamps to provide diffuse white light as an illumination source. Coherent laser light has also been recently implemented as the basis for diagnostics used in the study of ejecta [16] and debris [17] phenomena.

The LSL system offers several operational advantages over the conventionally used high-speed imaging techniques. Flash X-rays require extensive safety measures (given the aggressive radiation hazard) and therefore can be expensive to acquire large data sets. The LSL system currently uses 600 mW (or less) of laser illumination and therefore represents less of a safety hazard. Once installed, the LSL system is very inexpensive for continued operation.

Additionally, unlike many other techniques, the LSL system enables continuous high-intensity illumination of the target. The laser can be turned and left on for the duration of the experiment, enabling a simpler system triggering setup. This system is therefore advantageous for facilities without a reliable method to pre-trigger the illumination source. The constant illumination of the target also reduces operational complexity of the imaging system compared to pulsed laser photography systems [18].

Furthermore, the use of a coherent light source enables the measurement of additional phenomena, such as rarified atmosphere shock waves, which are immeasurable with other techniques. The use of coherent light allows the LSL system, with small modification, to be used for several interferometry techniques such as Schleiren imaging [19] and Coherent Gradient Sensing [20] to measure the impact phenomena. Collimated, coherent light has also been used in the SPHIR facility [21] to observed and characterize dynamic crack growth induced by hypervelocity impact in transparent materials. Lastly, the use of directed (collimated), monochromatic light does not interfere with any simultaneous spectroscopic measurements of the impact event during experiments.

3.1.1. System hardware

The Laser Side-Lighting system produces side-profile shadowgraphs using the Cordin 214-8 gated, intensified CCD camera. The Cordin camera contains 4 double-exposed CCD sensors to provide 8 images with 1000 × 1000 pixel resolution. The camera is capable of providing exposure and inter-frame times as low as 10 ns. The second exposure recorded on a given CCD must be delayed by at least 3.7 μs from the first exposure to allow the corresponding micro-channel plate (MCP) intensifier to reset. However, four consecutive images may be obtained by using each of the four CCDs once with a maximum framing rate of 50×10^6 fps.

A Coherent Verdi V6 diode-pumped solid-state laser is used to provide 532 nm (continuous wave) light as the illumination source. The laser beam is expanded to a 100 mm diameter collimated beam using two Keplerian beam expanders and then directed into the target tank. A large mirror is used to steer the laser illumination toward an imaging solution consisting of a Keplerian beam reducer, a focusing lens, and the Cordin camera's field lenses. The Verdi V6 laser is capable of producing 6 W of illumination intensity. The cross-section spatial intensity profile of the laser beam is approximately Gaussian. A more uniform intensity can be delivered to the ultra-high-speed camera through isolation of the laser beam's center and removal of the less-bright perimeter of the beam. Given that a small fraction (approximately 10%) of the available laser power is required to provide sufficient illumination intensity, the most-radial portions of the incident laser beam can be discarded. Therefore, a more uniform illumination source is achieved through over-expansion of the beam before re-collimation in the second Keplerian beam expander.

3.1.2. System setup and specifications

The laser illumination provided by the Verdi V6 laser is delivered into the target tank orthogonal to the impactor velocity vector.

Fig. 7 provides a conceptual illustration of the LSL system setup. The primary distinction of this method from flash X-ray is that the shadowgraphs generated by this method are produced by the absorption and diffraction of laser illumination by debris particles and subsequent interference of the coherent light. Constructive interference of the collimated laser source is created by gradients in the index of refraction corresponding to gradients in density, pressure, and temperature of the atmosphere surrounding the debris.

The current maximum field of view with this system is defined by the diameter of the expanded laser beam: 100 mm. To utilize all of the pixels in the square 1000 × 1000 pixel CCDs of the Cordin camera, the field of view can be adjusted to a square of approximately 70 mm × 70 mm. This corresponds to an image resolution of approximately 0.07 mm/pixel. Finer resolutions and smaller fields of view with higher image resolution are also possible. Fig. 8 provides an example sequence of images taken with the LSL system for a 0.5 mm thick 6061-T6 aluminum target plate impacted by a 5.5 mg (1.8 mm diameter) Nylon 6/6 cylinder at 5.84 km/s. A laser power of 600 mW is adequate to observe the hypervelocity impact event with exposure times as small as 10 ns. Furthermore, the short exposure time coupled with the collimated illumination source prevents the observed impact phenomena from being masked by camera pixel saturation from the impact flash.

As with the Photron fast camera used to measure impact speed, the Cordin camera used in the LSL system is triggered by the impact flash at the target. This method is robust and consistent; however, it has an inherent limitation: there is a short delay between first contact with the target and the development of an impact flash sufficiently bright to register on the photodiode. This creates an uncertainty in the time of initial contact between impactor and target. However, the time between the camera images is known very accurately (with an uncertainty less than 10 ns) and facilitates the accurate measurement of debris cloud evolution. Therefore, the times shown in Fig. 8 correspond to the time after triggering, and not the time after impact. Triggering of the LSL system is not limited to this triggering method and other triggering systems, such as a velocity comparator, could be used if available.

Furthermore, the use of collimated, coherent light in the LSL system enables the observation of additional impact features in experiments where the atmospheric pressure in the target chamber is increased above the nominal 1 mmHg. At higher pressures, waves emanating from the impact site are visible much like those observed in Schleiren shadowgraphs. The observation of these phenomena is enabled by strong gradients in the index of refraction of the rarefied atmosphere constructively interfering with the coherent light source. An example of this observation is provided in Fig. 9 for a $h = 0.5$ mm plate impacted at 4.7 km/s in 50 mmHg atmospheric pressure. A slight defocussing of the LSL system greatly increases the contrast in the observed shock waves. Measurement of these waves can enhance understanding of the temporal sequence of the impact phenomena and provides a further basis for comparison with other metrics discussed herein.

3.2. Near-IR imaging and UV–vis spectroscopy

There have been a number of previous investigations to examine hypervelocity impact-induced light emission. Perhaps the most significant experiments to observe the impact-induced emission have been carried out by Schultz and Sugita [22–32]. These studies investigated a number of different impactor materials (aluminum, copper, Pyrex, quartz, polycarbonate, etc.) and target materials (dolomite, calcite, sand, dry ice, water, copper, etc.) and were able to obtain atomic and molecular emission spectra with moderate time and spectral resolution. The experiments also ascertained impact-induced vapor temperatures, measured significant changes in the phenomena when changing impact angle and spectroscopically analyzed the atmospheric interactions of impact-induced vapor clouds.

In order to more closely examine the hypervelocity impact emission, the SPHIR facility utilizes two Princeton Instruments

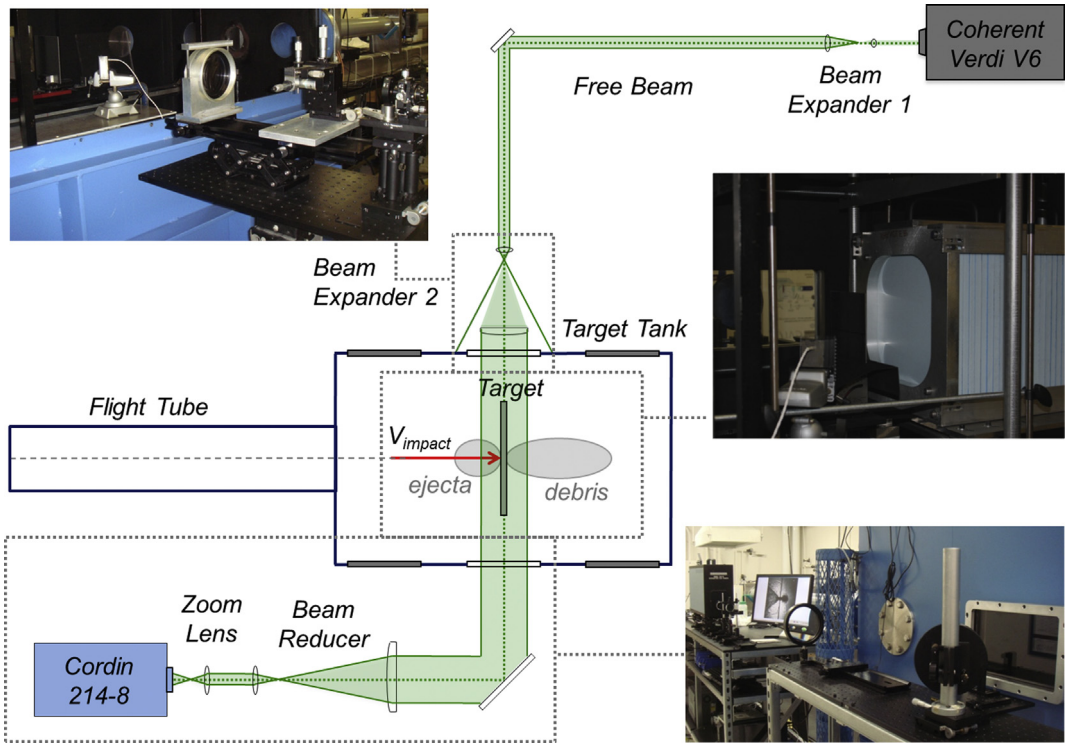

Fig. 7. Illustration of the Laser Side-Lighting system and various views (illustration not to scale).

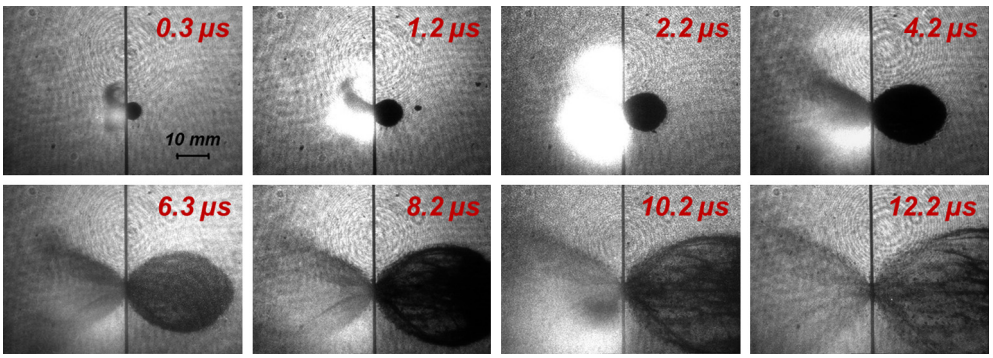

Fig. 8. A sequence of Laser Side-Lighting images with the ultra-high-speed camera taken for a 0.5 mm thick 6061-T6 aluminum target plate impacted by a 1.8 mm diameter, 5.5 mg Nylon 6/6 cylinder at 5.84 km/s. Times displayed are the effective time of the image after triggering.

spectrograph systems. Both systems employ an Acton SP2560 spectrograph; the first of which utilizes a high-speed OMA-V camera (minimum exposure time 1 μs), with a 320 × 256 pixel liquid nitrogen cooled InGaAs detector array, to measure the near-IR emission (from 0.9 μm to 1.7 μm) during each impact event. The second spectrograph couples a high-speed PI-MAX 3 camera (minimum exposure time 28 ns) with an intensified 1024 × 256 pixel CCD detector to observe the UV–visible emission (from approximately 275 nm–825 nm) of each event. The OMA-V and PI-MAX 3 camera/spectrograph systems are operated by the WinSpec32 and LightField software (provided by Princeton Instruments) respectively. Both spectrograph systems are able to record either a single image or spectrum of the emission by utilizing an internal directing mirror or a 150 g/mm, 600 g/mm or 1200 g/mm grating, enabling observation of broad spectra or individual spectral bands. Currently, the OMA-V camera is primarily employed for imaging, whilst the PI-MAX 3 system is used to obtain emission spectra.

The two spectrographs systems are mounted above the SPHIR target chamber, as shown in Fig. 1, and oriented to view the impact at an angle of approximately 27° from vertical. The field of view for the near-IR camera may also be altered by utilizing lenses with focal lengths ranging from 8 mm to 90 mm, yielding fields of view between 60.0 cm × 48.5 cm and 5.3 cm × 4.3 cm respectively. This camera nominally utilizes a 25 mm lens giving a field of view of 25.1 cm × 20.0 cm. The UV–vis camera's field of view is determined both by the camera lens and the spectrograph slit width (variable) and height (fixed). In general, a 20 mm focal length lens is used with a slit width of 100 μm, yielding a field of view of approximately 1.3 cm (width) × 12.7 cm (height). Both the near-IR and UV–vis spectrograph systems may be used with a wide variety of impactors, target materials and target configurations.

The OMA-V camera is currently used to acquire a near-IR image (0.9 μm–1.7 μm) of the impact-induced emission with 320 × 256 pixel resolution. These images provide a distribution of all near-IR emission from both the uprange and downrange phenomena. Fig. 10 shows the near-IR image of a 1.8 mm Nylon 6/6 projectile impacting a 1.5 mm thick aluminum target at an angle of 0° from vertical. The impact velocity was 5.22 km/s and the chamber pressure was 1.0 mmHg. The image was captured from 0.3 μs after impact with an exposure time of 5 μs. The image therefore displays the total integrated emission seen by the detector array during these 5 μs. The field of view of the image is 25.1 cm (width) × 20.0 cm (height). The target position (overlaid) and direction of impact are also shown and artificial color is added to improve clarity. As observed in Fig. 10, the near-IR image reveals a large expanding uprange cloud, containing a bright exterior and dark center, and a smaller downrange cloud, which represents the emitting material that has passed through the target. As shown in Fig. 10, the downrange material has not expanded as far as the uprange cloud, due to the time required to perforate the aluminum target and the relative velocities of the two clouds.

The PI-MAX 3 system is currently utilized to obtain UV–vis emission spectra of the impact-induced vapor/plasma cloud. The wavelength range of the spectrum obtained is determined by a chosen central wavelength (within the spectral range of the camera's detector) and the spectral coverage of the diffraction grating. The wavelength coverage is 351 nm and 41 nm for the 150 g/mm

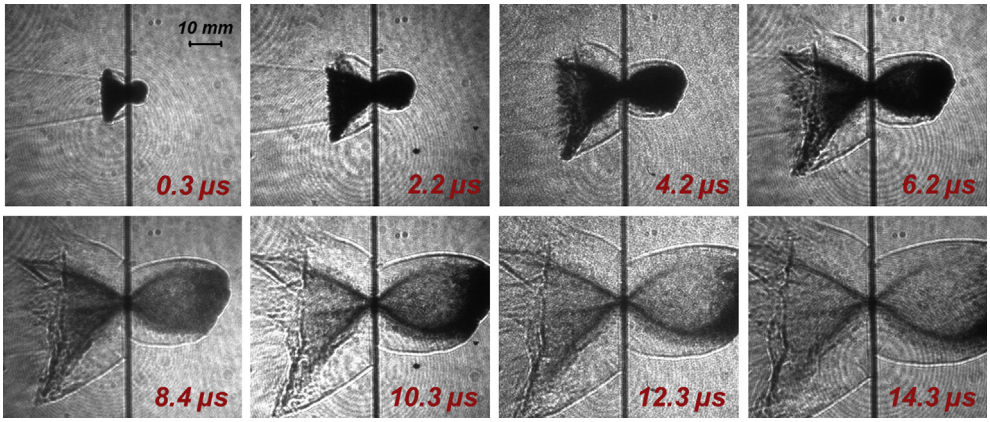

Fig. 9. A sequence of Laser Side-Lighting images taken with the ultra-high-speed camera for a 0.5 mm thick 6061-T6 aluminum target plate impacted by a 1.8 mm diameter, 5.5 mg Nylon 6/6 cylinder at 4.87 km/s at 52.0 mmHg target chamber pressure. Times displayed are the effective time of the image after triggering.

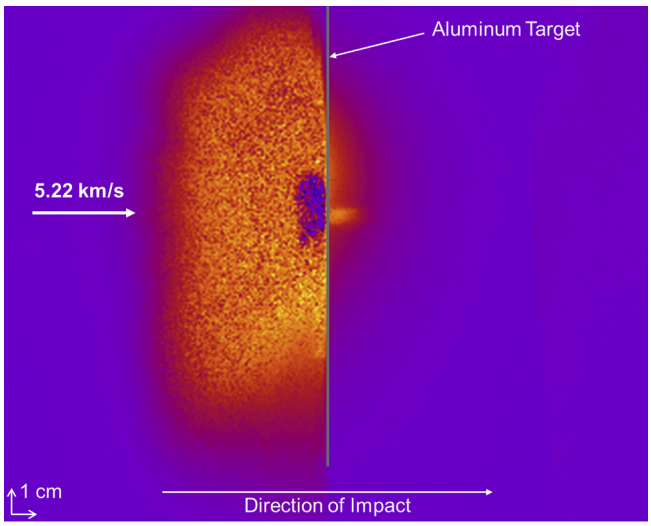

Fig. 10. Near-IR image of a 1.8 mm Nylon 6/6 projectile impacting a 1.5 mm thick aluminum target at an angle of 0° from vertical. The impact velocity was 5.22 km/s and the chamber pressure was 1.0 mmHg. The image was captured from 0.3 μs after trigger with an exposure time of 5 μs. The field of view of the image is 25.1 cm × 20.0 cm (W × H). The target position and direction of impact are indicated and artificial color is added to improve clarity. (For interpretation of the references to color in this figure legend, the reader is referred to the web version of this article.)

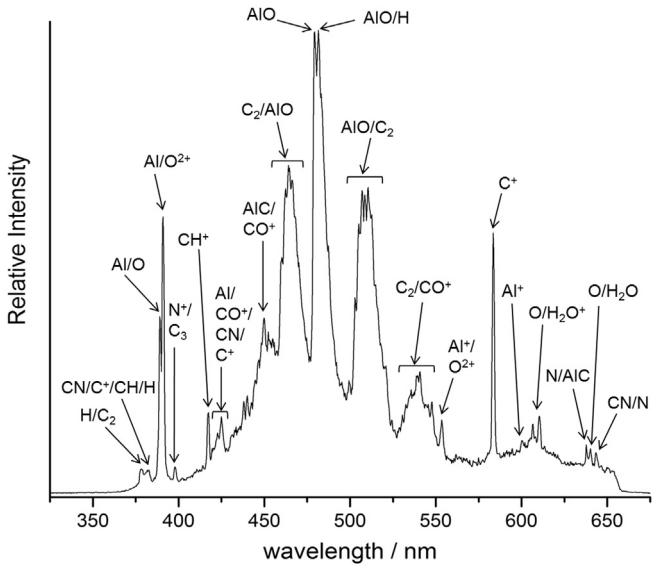

Fig. 11. UV–vis spectrum of a 1.8 mm Nylon 6/6 projectile impacting a 1.5 mm thick aluminum target at an angle of 0° from vertical. The impact velocity was 5.56 km/s and the chamber pressure was 1.0 mmHg. The spectrum was taken from 8.3 μs after trigger and with an exposure time of 2 μs. The spectrometer slit field of view was positioned approximately 2.5 cm in front of the target. The wavelength range was from 324.86 nm to 674.92 nm with an instrument defined spectral resolution of 1.3 nm. Preliminary assignments for each observed spectral band are indicated [33,34].

and 1200 g/mm diffraction gratings respectively. The spectral resolution is determined by both the diffraction grating dispersion and the slit width of the spectrograph. A slit width of 100 μm is most commonly used, which corresponds to a spectral resolution of 1.3 nm and 0.15 nm for the 150 g/mm and 1200 g/mm diffraction gratings respectively. The spectrograph slit may be positioned to allow measurement of either the uprange or downrange vapor/plasma cloud emission. The PI-MAX 3 camera system is calibrated using the Princeton Instruments Hg/Ne–Ar light source and the automated IntelliCal calibration procedure within the LightField software. This procedure allows a broad spectral calibration of approximately ±0.08 nm for the 150 g/mm diffraction grating and a fixed spectral calibration of ±0.01 nm for the 1200 g/mm grating. The total wavelength uncertainty includes contributions from both the calibration uncertainty and the wavelength accuracy of the spectrograph, which are approximately ±0.22 nm and ±0.20 nm for the 150 g/mm and 1200 g/mm grating respectively.

Fig. 11 shows a UV–vis spectrum of a 1.8 mm Nylon 6/6 projectile impacting a 1.5 mm thick aluminum target at an angle of 0° from vertical. The impact velocity was 5.56 km/s and the chamber pressure was 1.0 mmHg. The spectrum was captured 8.3 μs after trigger and with an exposure time of 2 μs. The spectrometer slit field of view was positioned approximately 2.5 cm in front of the target to measure the uprange vapor/plasma cloud emission. The wavelength range was from 324.86 nm to 674.92 nm with an instrument defined spectral resolution of 1.3 nm. Analysis of the impact emission spectra yields information regarding the atomic and molecular species present in the vapor/plasma cloud and the relative intensities of their emission. Preliminary assignments for each observed spectral band in Fig. 11 are indicated and show evidence of species originating from both the target (aluminum) and projectile (Nylon 6/6) materials. As shown, there are several possible assignments for many of the observed spectral bands, due to the moderate resolution of the spectrum. For future investigations, the use of the 1200 g/mm diffraction grating may improve the resolution of the spectrometer sufficiently in order to establish more conclusive assignments, if the current widths of the spectral bands are not determined solely by the Stark broadening of the vapor/plasma cloud. It may also be possible to measure the Stark broadening of a specific spectral band in order to approximately calculate the pressure of the vapor/plasma cloud.

Further investigations are currently in progress to more closely examine the nature (atomic and molecular species, emission lifetimes, expansion direction and velocity, etc.) of the vapor/plasma cloud using a variety of initial conditions including impact velocity, target thickness and target obliquity.

4. *Post mortem* diagnostics

The *in situ* high-speed diagnostics presented herein are complemented by two *post mortem* diagnostics. The first diagnostic, back-surface profilometry of the target, characterizes the permanent back-surface deformation of the target. The second diagnostic, a debris capture system located behind the target plate, characterizes the debris behavior and debris lethality produced in each experiment.

4.1. Post mortem target back-surface profilometry

The Optimet MiniConoscan 3000 Laser Conoscope is used to conduct *post mortem* target specimen profilometry [5]. This instrument produces a three-dimensional {x,y,z} Cartesian coordinate map describing a surface of a target with 6–10 micron precision in the in-plane directions and approximately 25 micron precision in the out-of-plane direction. This allows for quantitative measurements of deformation features, such as target perforation area or the surface slope field. An example of a measurement taken with the Conoscope (for the same experiment as shown in Fig. 8) is presented graphically in Fig. 12.

4.2. Debris capture system

The nature of the debris thrown downrange from an impacted target is not only of interest for fundamental understanding of the damage mechanics produced by hypervelocity impact but also of significance to the engineering of shield systems on spacecraft. The composition, number, size, velocity vector and energy of the

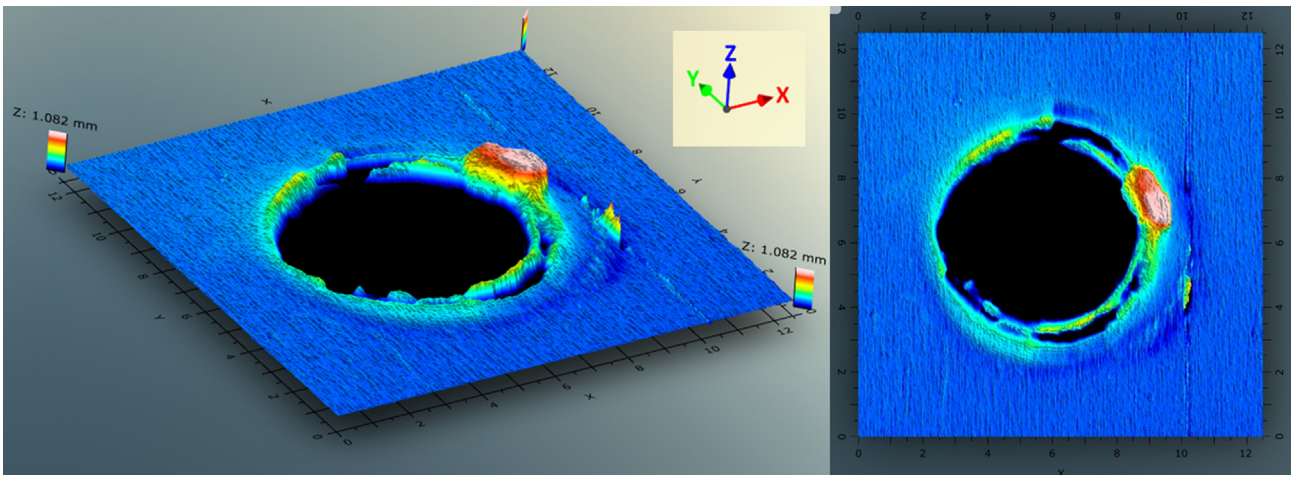

Fig. 12. Conoscope generated measurements of out-of-plane displacement for the target presented in Fig. 8. Colors depict relative out-of-plane z-position, with white corresponding to 1.1 mm above dark blue.

fragments in the debris cloud result from the processes involved in the penetration and perforation of the target. Spacecraft shielding is designed to "protect" against a certain probability of particle impact, i.e. a defined maximum combination of particle mass and velocity, typically the incident kinetic energy. Overmatching threats can defeat the shield and result in perforation and the formation of a debris cloud that hits protected components. The margin of safety of a shield system is, in part, dependent on the lethality of this debris cloud.

A capture pack system, as seen in Fig. 2, was designed and constructed to measure some of the important characteristics of the debris cloud thrown behind the target. The pack consists of alternating, 12 mm thick plates of low density (0.027 g/cm^3) polystyrene foam and 0.2 mm thick sheets of colored cellulose acetate plastic. The areal density of each foam plate is 0.035 g/cm^2 and the areal density of each plastic sheet is 0.016 g/cm^2. The stack of plates and sheets is aligned by precision ground rods that pass through two diagonal corners of the stack and is slightly compressed by four threaded rods that pass between the front and back aluminum plates. The front (uprange) face of the capture pack is located 127 mm behind the back (downrange) surface of the target. The precision of alignment of this fixture is sufficient to ensure that positions on the plates and sheets can be determined to within 1 mm of the hit position on the target. The geometry and coordinate system of the capture pack system is presented in (Fig. 13).

After the target is impacted, the pack is removed from the target chamber and disassembled. Most debris material is contained within the foam plates but often particles will be trapped at the interface between a foam and plastic layer. Recovery of the debris particles is simple but time consuming.

Measurement of the debris patterns are accomplished using a light table, transparent alignment plate and digital camera. Each plastic sheet is placed on the alignment plate resting on the light table and a coordinate system is established using fiducial marks, which correspond to the ground alignment rods of the test fixture. A photograph is taken of the entire sheet and an image analysis program (Image J) is used to characterize various properties of the perforation pattern in each sheet, e.g. number of perforations, location of each perforation, perforation area, etc. These measurements are easily made by inverting and thresholding the digital image such that the perforation holes are black (grayscale = 0) on a white (grayscale = 255) background. Digital photographs of the target facing surface of the first foam plate are also taken using angled illumination. Often these can be analyzed in the same fashion describe above for the plastic sheets.

Analysis of the capture pack measurements provides considerable information about the nature of the debris cloud produced by perforation of the target. Some examples of these analyses follow in the next section. Since positions on each sheet/plate are referenced to the hit position on the target, the angular distribution of the individual debris particles can be determined (see Fig. 19). The penetration path length of a given particle through the pack is a measure of the total areal density of material required to bring the debris particle to rest, which is a measure of its penetration capability (lethality) and related to the particle's mass, speed and penetrating cross-section (see Fig. 18). The maximum depth of debris particle penetration into the pack is a measure of the lethality of the debris cloud produced by that target and impact condition.

5. Analysis and results

5.1. Determination of trigger delay

Analysis of the ejecta and debris propagation using the LSL system can provide an estimate of the delay between the impact and the instrumentation trigger signal. The one-dimensional

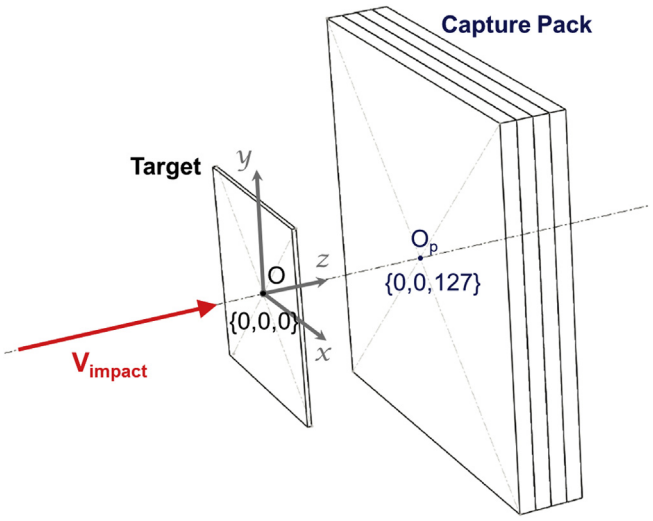

Fig. 13. Schematic of the coordinate system describing the target plate and capture pack system placed 127 mm behind the target.

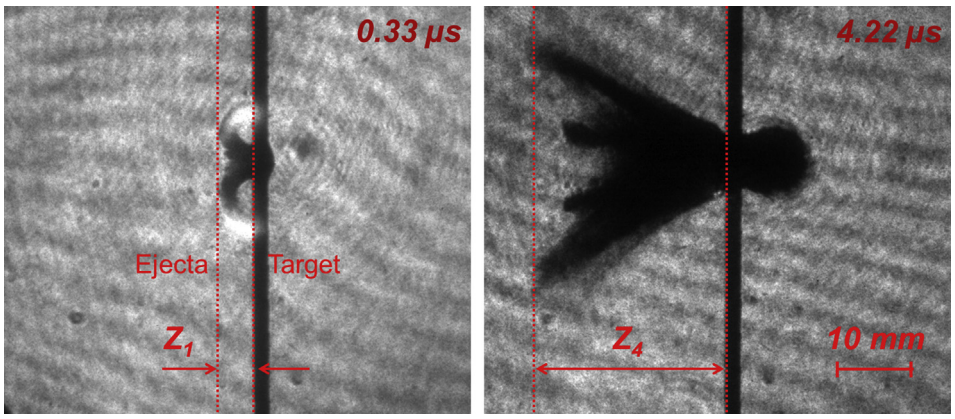

Fig. 14. Example measurements of the position of debris ejecta uprange following an impact. Times displayed are the effective time of the image after triggering. Such measurements are used to compute the z-component of the impact's front-ejecta velocity, which is then used to accurately measure t_{trig}. Ejecta images shown for a $h = 1.5$ mm thick 6061-T6 aluminum target plate impacted by a $D = 1.8$ mm Nylon 6/6 ($L/D = 1$) right cylinder at 6.32 km/s.

velocity in the z-direction of the front-ejecta (debris ejected uprange, opposite of the impact vector) is measured and then used to estimate the time of impact. To do so, the z-position of the most uprange front-ejecta is first determined [35] with respect to the impacted surface. Fig. 14 provides an example of the measurement of the forward-most front-ejecta position in LSL images for a $h = 1.5$ mm thick 6061-T6 aluminum target plate impacted by a $D = 1.8$ mm Nylon 6/6 ($L/D = 1$) right cylinder at 6.32 km/s.

The one-dimensional front-ejecta velocity (v_{ejecta}) in the z-direction is then estimated using least-squares linear regression analysis of the measured sequential front-ejecta positions. Fig. 15(a) provides an example of the z-position vs. image timing for the previously presented example (Fig. 14). The time required for the ejecta to propagate from the impacted target surface to the observed position can then be estimated for the first LSL image. Subtracting the effective time t_1 of the LSL image ($t_{image} = t_{del} + t_{exp}$) then provides the trigger delay time t_{trig}, assuming a constant front-ejecta speed and immediate ejecta of particles at impact. This approximation is described by Eq. (4) and graphically illustrated in Fig. 15(b).

$$t_{trig} = \frac{Z_1}{v_{ejecta}} - t_1 \tag{4}$$

$$\varepsilon_t = \sqrt{\left(\frac{\partial t_{trig}}{\partial Z_1}\varepsilon_{Z_1}\right)^2 + \left(\frac{\partial t_{trig}}{\partial v_{ejecta}}\varepsilon_{v_{ejecta}}\right)^2 + \left(\frac{\partial t_{trig}}{\partial t_1}\varepsilon_{t_1}\right)^2} \tag{5}$$

The measurement of individual debris particles in consecutive frames is not feasible with the current LSL system. However, the measurement of the forward-most aggregate position of (many) ejecta particles to compute a one-dimensional velocity component mitigates this limitation. Such a measurement in one-direction also reduces the dimensionality of the uncertainty in the definition of the debris position: errors in the identification of the position of ejecta are accounted for in only one-direction. The relative positions of the forward-most front-ejecta with respect to the target plate are measured with uncertainties of 8 pixels. Gating signals from each instrument are precisely monitored allowing t_{del} and t_{exp} to be measured with an uncertainty of only 10 ns. For typical ejecta velocities observed, these uncertainties produce an RMS uncertainty (Eq. (2)) of the ejecta speed of approximately 5%. The estimate of the trigger time t_{trig} uncertainty is then computed given Eq. (5), with typical values ranging between 100 and 200 ns. Furthermore, strong linear regression correlation coefficients (typically 0.98 or above) between the measured z-positions and image times supports the accuracy of this method.

5.2. Results

The suite of instrumentation described herein provides a comprehensive, quantitative description of impact phenomena during each experiment. Results from each of the described instruments are described herein for an experimental result for a 1.5 mm thick 6061-T6 aluminum plate impacted at 6.32 km/s by a 5.5 mg Nylon 6/6 1.8 mm diameter right cylinder.

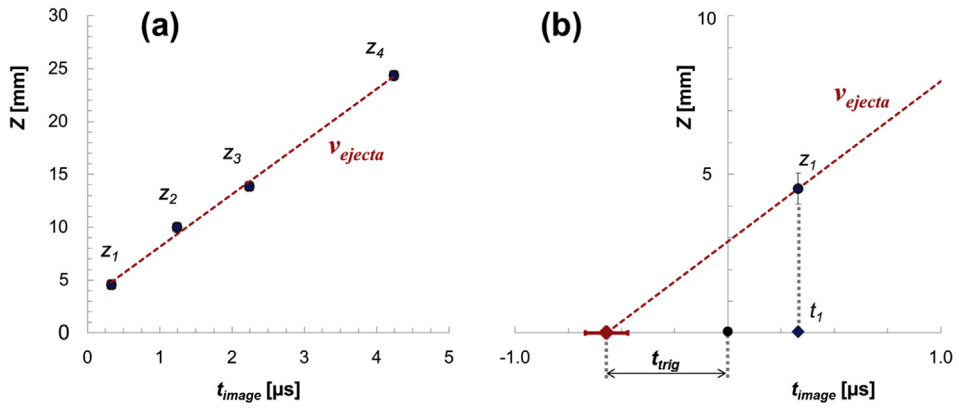

Fig. 15. (a) Z-position vs. image time measured for the front-ejecta presented in Fig. 14. Least-squares linear regression is then used to estimate the one-dimensional front-ejecta velocity, v_{ejecta}. (b) Geometrical representation of the use of v_{ejecta} to determine the trigger delay time t_{trig}, given the front-ejecta position measured in the first image.

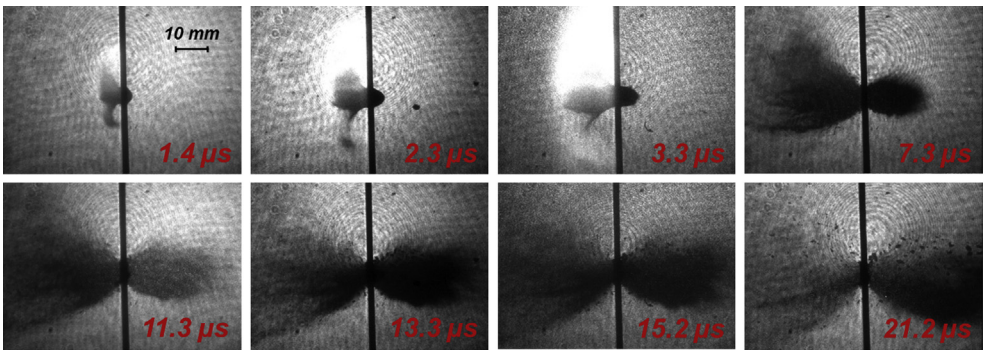

Fig. 16. A sequence of Laser Side-Lighting images taken with the ultra-high-speed camera for a 1.5 mm thick 6061-T6 aluminum target plate impacted by a 1.8 mm diameter, 5.5 mg Nylon 6/6 cylinder at 6.32 km/s. Times shown are the time after impact, given the described measurement of the trigger signal delay.

For the considered experiment, Fig. 16 presents the LSL system results which describe the temporal formation and evolution of the debris cloud thrown downrange behind the target. Using the technique described in the previous section, the delay between impact and trigger signal is determined to be 1.1 ± 0.1 μs. Accordingly, the times presented in Fig. 16 are in reference to the impact. The distribution of ejected material in Fig. 16 is different than observed in Fig. 14 for results from a separate experiment with the same target thickness and impact velocity. This disparity is attributed to the tumbling of the cylindrical impactor.

When the debris front is best defined, i.e. time after impact <5 μs, an edge-finding algorithm (previously described [35]) is implemented to identify the position of the debris in subsequent images. The location of the debris front is estimated within 5 pixels or less that yields an accuracy of position of ±0.3 mm. Given the very small temporal uncertainty associated with Cordin camera (less than 10 ns), measurement of the debris velocity can be computed with an accuracy of ±0.1 km/s Fig. 17 provides an example of the measured debris front position during the early stages of debris cloud formation for the same considered experiment. For this experiment, the velocity collinear with incident impact velocity is 1.9 km/s. This measurement is one example of a metric which can be used to compare with the predictions of numerical simulations [36] and to help quantify their uncertainty [37].

Capture packs located behind the target of each test collect the downrange debris thrown from each target tested and record the individual depths of penetration of each debris particle and the direction penetration (their penetration vectors). Such measurements compliment the measurements of debris cloud speed and trajectory discussed above and can be compared with them. Fig. 18 provides an example of capture pack data for the considered experiment and describes the xy hit position of individual debris particles in the layered medium of the capture pack. As observed, the most aggressive (largest and fastest) debris particles are asymmetrically distributed. The deepest penetrating particles are spread near horizontally and biased below the horizontal plane of impact. This data provides a metric for comparison to simulations by providing information regarding the number and distribution of large debris particles. Furthermore, the three-dimensional information regarding the trajectory of the debris particles can be compared to the two-dimensional debris cloud image produced with the LSL system.

Using the xy hit position data, the angular and radial distributions of the debris cloud can be computed for each layer of the acetate film in the capture pack. Fig. 19 provides an example of such analysis for the first layer (P1) in the considered experiment. The

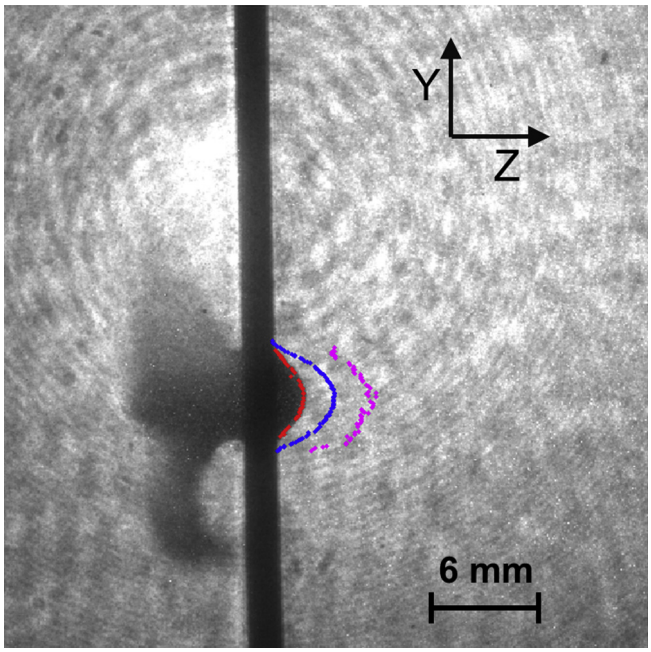

Fig. 17. The evolution of the debris front presented in Fig. 16, as measured by the Laser Side-Lighting system. Image taken at 0.3 μs with debris positions measured for 1.2 μs and 2.2 μs also shown.

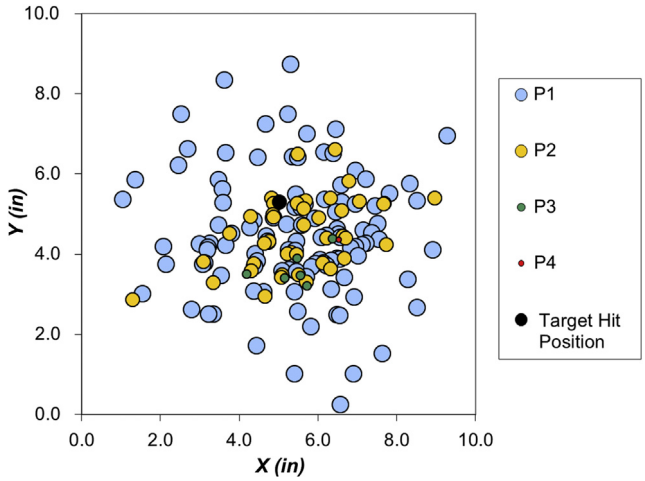

Fig. 18. Spatial distribution of perforations in the capture pack system generated by the debris produced in the experiment presented in Fig. 16.

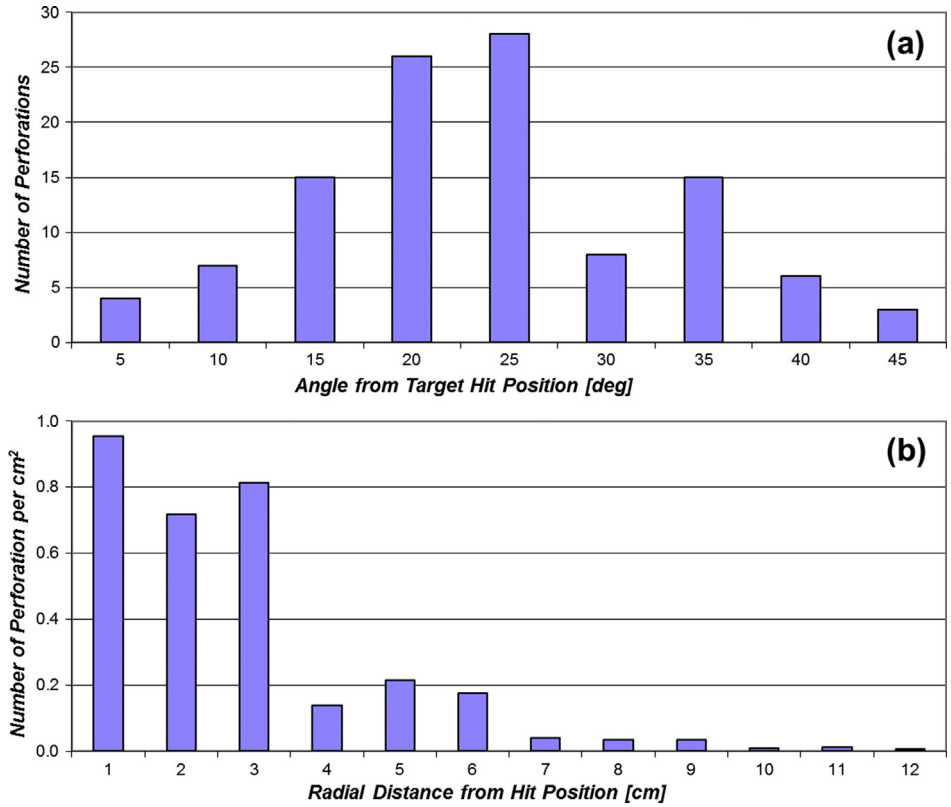

Fig. 19. Angular and radial distribution of perforations in the capture pack system generated by the debris produced in the experiment presented in Fig. 16.

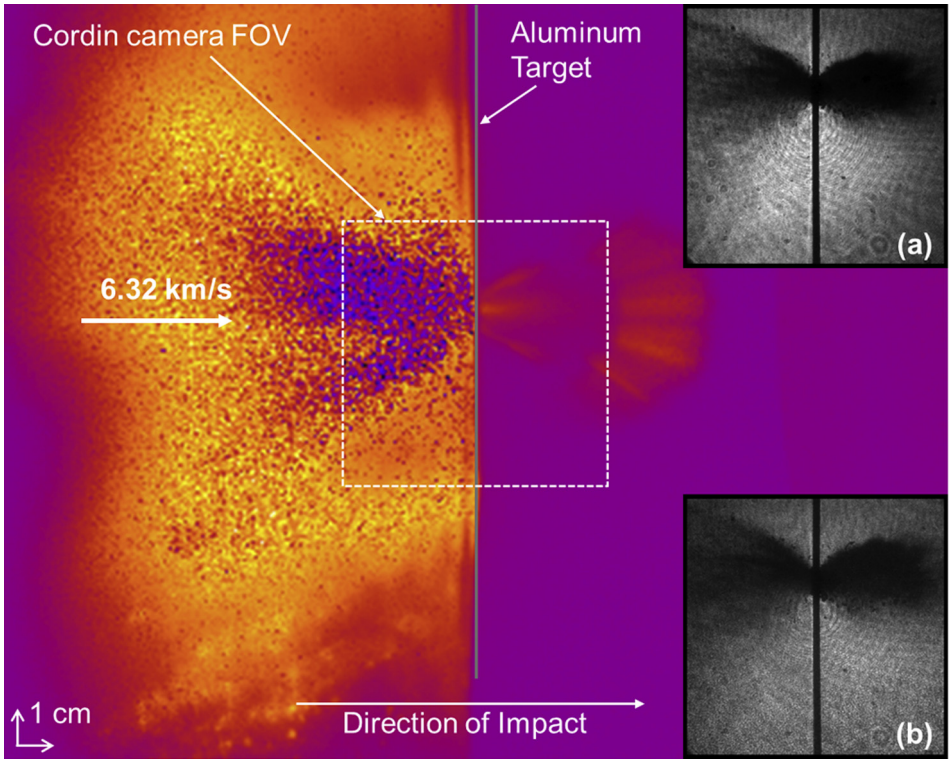

Fig. 20. Near-IR image of a 1.8 mm Nylon 6/6 projectile impacting a 1.5 mm thick aluminum target at an angle of 0° from vertical. The impact velocity was 6.32 km/s and the chamber pressure was 1.2 mmHg. The image was captured from 12.3 μs after trigger with an exposure time of 2 μs. The field of view of the image is 25.1 cm × 20.0 cm (W × H). Two LSL images corresponding to the approximate start time (a) and end time (b) of the 2 μs IR camera exposure are overlaid with the field of view of the Cordin camera also shown. The target position and direction of impact are indicated and artificial color is added to improve clarity. (For interpretation of the references to color in this figure legend, the reader is referred to the web version of this article.)

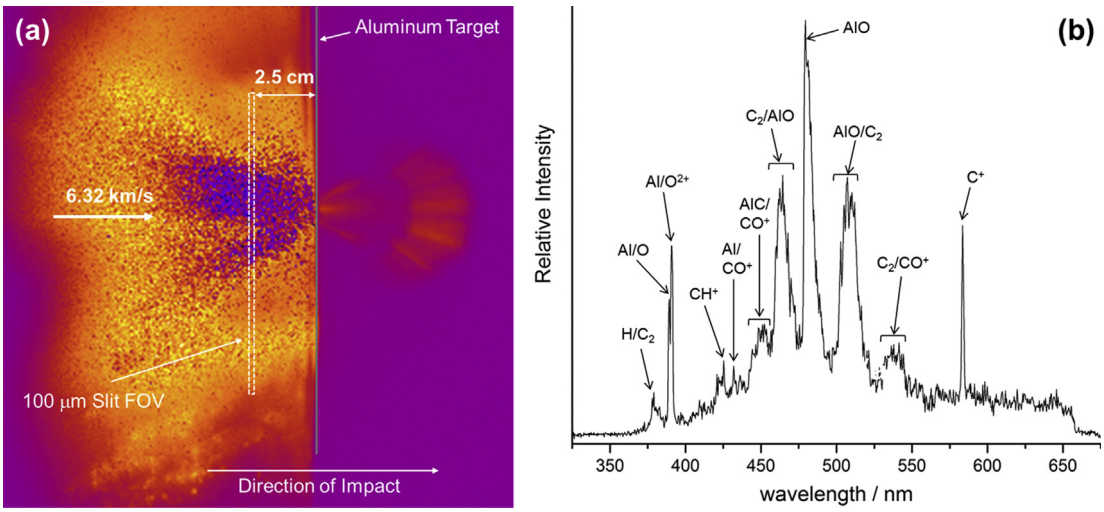

Fig. 21. (a) The approximate field of view of the UV–vis spectrograph slit (100 μm) is indicated on the cropped near-IR image. The slit was positioned approximately 2.5 cm in front of the target the target position and direction of impact are indicated and artificial color is added to improve clarity. (b) The corresponding UV–vis spectrum of a 1.8 mm Nylon 6/6 projectile impacting a 1.5 mm thick aluminum target at an angle of 0° from vertical. The impact velocity was 6.32 km/s and the chamber pressure was 1.2 mmHg. The spectrum was taken from 12.3 μs after trigger and with an exposure time of 2 μs. The wavelength range was from 324.86 nm to 674.92 nm with an instrument defined spectral resolution of 1.3 nm. Preliminary assignments for each observed spectral band are indicated [33,34]. (For interpretation of the references to color in this figure legend, the reader is referred to the web version of this article.)

angular distribution is computed by binning the number of perforations contained in 5 degree sectors surrounding the impact position. The radial distribution is computed by considering the number of perforations in annular areas centered about the impact position. For any experiment, changes in the angular distribution in subsequent layers can be used to evaluate whether the trajectory of the debris particles remains straight while decelerating through the capture pack. Additionally, for multiple experiments, the effect of impactor tumbling can be quantified through analysis of the radial and angular distributions of debris particles.

As previously discussed, the near-IR and UV–vis spectrograph and camera systems further complement these results by providing images and spectra of the diffuse vapor/plasma cloud that accompanies the observed ejecta and debris. Fig. 20 shows the near-IR image of the vapor cloud observed in the same impact event illustrated in Figs. 16,17. Two LSL images corresponding to the approximate start time (a) and end time (b) of the 2 μs IR camera exposure are overlaid with the field of view of the Cordin camera also indicated.

These images illustrate the distinctly different phenomena observed using the LSL and IR imaging.

In particular, the IR image shows two separate downrange emitting regions consisting of distinct jets of emitting vapor, which are not shown in any of the LSL images (Fig. 16). The uprange emitting vapor shown in Fig. 20 also demonstrates the clear difference in the ejecta observed by the LSL and IR imaging techniques. The size of the uprange cloud is significantly larger than the uprange ejecta observed using the LSL system (Fig. 16). These observations indicate that the emitting cloud is a distinctly different phenomenon to both the uprange ejecta and downrange debris observed using the LSL technique. It seems most likely that the emitting phenomenon is a relatively diffuse vapor/plasma cloud, similar to that observed by Schultz [22–32]. Additionally, the outer edges of both the bright and dark areas of the vapor/plasma cloud have almost identical shapes, indicating the presence of a single uprange phenomenon.

Furthermore, both the emitting and darker areas are significantly larger than those observed in Fig. 10, due to the larger delay after the photodiode trigger (12.3 μs vs. 0.3 μs). This comparison suggests an expansion of the vapor cloud over time, perhaps similar to that observed in the LSL images. Unfortunately, a measurement of this expansion would require several experiments to be run under almost identical conditions, as the OMA-V camera is only capable of recording a single image of each impact. Further analysis of the emission intensities in the near-IR images will allow a measure of the vapor/plasma cloud energy and should offer additional information for the timing, velocities, trajectories, pressures and temperatures in such impact phenomena.

Fig. 21 shows the approximate field of view of the UV–vis spectrograph slit (100 μm) overlaid on the cropped near-IR image from Fig. 20. In this experiment the slit was positioned approximately 2.5 cm in front of the target to measure the uprange vapor/plasma cloud emission. The PI-MAX 3 camera captures all UV–vis emission that passes through the field of view of the spectrograph slit during the 2 μs exposure of the camera. Fig. 21 also presents the UV–vis spectrum resulting from the emission recorded using this spectrograph slit, over the same time exposure used in the near-IR image shown in Fig. 20. The spectrum again shows strong emission from several atomic and molecular species originating from both the target (aluminum) and projectile (Nylon 6/6) materials.

6. Conclusion

The diagnostics discussed in this paper are routinely employed in every experiment conducted at the SPHIR facility. The utilization of a coherent, collimated illumination source for imaging of debris enables the use of simultaneous measurements of phenomena with near-IR and UV–vis spectrograph systems. This suite of instrumentation provides multiple complementary measurements that facilitate the characterization of multiple impact phenomena in a single experiment. As such, the extensive instrumentation of the facility maximizes the data output from each experiment and provides a high return on investment given the fixed costs of each shot. Because of this, experimental campaigns of several shots yield very comprehensive data sets on a host of phenomena. Such data sets are useful for the validation of models, particularly those with “multi-scale” features. The current campaign is studying the phenomena associated with the impact of nylon cylinders on aluminum targets. However, the diagnostic capabilities and techniques described can

be used with a wide variety of impactors, target materials, and target configurations to investigate any number of engineering and scientific problems.

Acknowledgments

This material is based upon work supported by the Department of Energy National Nuclear Security Administration under Award Number DE-FC52-08NA28613. The authors would also like to thank Mike Mello for his assistance with the opto-mechanical design of the LSL system, Petros Arakelian for his assistance in installing the optical benches and safety features, and Phillip Ou for compiling the capture pack data.

References

[1] Arnold JO, Goldstein HE, Rigali DJ. "Follow the TPS" appendix IV, F2 report of the Columbia Accident Investigation Board 2003.
[2] Personal communication. Adams MA. NASA Jet Propulsion Laboratory.
[3] Christiansen E. Meteoroid/debris shielding, NAS TP-2003–210788 2003.
[4] Davis BA. Thermal, radiation and impact protection systems (TRIPS), NASA JSC HITF internal report, hypervelocity impact test summary for FY 06.
[5] Mihaly JM, Lamberson LE, Adams MA, Rosakis AJ. A low cost, small bore light-gas gun facility. In: Proceedings of the 11th hypervelocity impact symposium 2010. p. 675–86.
[6] Grosch DJ, Riegel JP. Development and optimization of a "Micro" two-stage light-gas gun. Proceedings of the 1992 hypervelocity impact symposium.
[7] Konrad CH, Hollenbach RE. Techniques for determining velocity and position of small hypervelocity spheres 1976. Sandia Laboratories internal report SAND75–0624.
[8] Prof. Hans Hornung (Graduate). Personal communication. Aerospace Laboratories California Institute of Technology.
[9] Piekutowski AJ. Characteristics of debris clouds produced by hypervelocity impact of aluminum spheres with thin aluminum plates. Int J Impact Eng 1993;14.
[10] Piekutowski AJ. Debris clouds produced by the hypervelocity impact of nonspherical projectiles. Int J Impact Eng 2001;26.
[11] Friend WH, Murphy CL, Gough PS. Review of meteoroid-bumper interaction studies at McGill University, NASA CR-54858.
[12] Kassel PC, DiBattista JD. An ultra-high-speed photographic system for investigating hypervelocity impact phenomena, NASA TN D-6128 1971.
[13] Francesconi A, Pavarin D, Giacomuzzo C, Angrilli F. Impact experiments on low-temperature bumpers. Int J Impact Eng 2006;33:264–72.
[14] Williamsen J, Howard E. Video imaging of debris clouds following penetration of lightweight spacecraft materials. Int J Impact Eng 2001;26.
[15] Putzar R, Schaefer F, Lambert M. Vulnerability of spacecraft harnesses to hypervelocity impacts. Int J Impact Eng 2008;35:1728–34.
[16] Hermalyn B, Schultz PH, Heineck JT. Early stage ejecta velocity distribution. In: 40th lunar and planetary science conference 2009.
[17] Zhang Q, Chen Y, Huang F, Long R. Experimental study on expansion characteristics of debris clouds produced by oblique hypervelocity impact of LY12 aluminum projectiles with thin LY12 aluminum plates. Int J Impact Eng 2008;35.
[18] Isbell WM. Historical overview of hypervelocity impact diagnostic technology. Int J Impact Eng 1987;5:389–410.
[19] Settles GS. Schleiren and shadowgraph techniques: visualizing phenomena in transparent media. Berlin: Springer-Verlag; 2001.
[20] Rosakis AJ. Two optical techniques sensitive to gradients of optical path difference: the method of caustics and the coherent gradient sensor (CGS). In: Epstein J, editor. Experimental techniques in fracture 1993. p. 327.
[21] Lamberson LE, Eliasson V, Rosakis AJ. In situ optical investigation of hypervelocity impact induced dynamic fracture. Exp Mechanics, Special Edition Dynamic Behavior of Materials 2011:1–10.
[22] Schultz PH, Adams MA, Sugita S. Impact flash spectroscopy. In: Lunar and planetary science conference (LPSC) XXVII 1996. p. 1149.
[23] Sugita S, Schultz PH, Adams MA. In situ temperature measurements of impact-induced vapor clouds with a spectroscopic method. In: LPSC XXVIII #1306 1997.
[24] Sugita S, Schultz PH. Spectroscopic observation of atmospheric interaction of impact vapor clouds. In: LPSC XXIX #1751 1998.
[25] Sugita S, Schultz PH. Spectroscopic measurements of vapor clouds due to oblique impacts. J Geophys Res-Planet 1998;103(E8).
[26] Sugita S, Schultz PH. Spectroscopic characterization of hypervelocity jetting: comparison with a standard theory. J Geophys Res-Planet 1999;104(E12).
[27] Sugita S, Schultz PH. Spectroscopic observation of chemical interaction between impact-induced vapor clouds and the ambient atmosphere. In: LPSC XXXI #2029 2000.
[28] Ernst CM, Schultz PH. Effect of initial conditions on impact flash decay. In: LPSC XXXIV #2020 2003.
[29] Eberhardy CA, Schultz PH. Looking inside the early-time radiation plume for hypervelocity impacts. In: LPSC XXXIV #2039 2003.
[30] Sugita S, Schultz PH, Hasegawa S. Intensities of atomic lines and molecular bands observed in impact-induced luminescence. J Geophys Res-Planet 2003;108(E8).
[31] Eberhardy CA, Schultz PH. Probing impact-generated vapor plumes. In: LPSC XXXV #1855 2004.
[32] Ernst MC, Schultz PH. Early-time temperature evolution of the impact flash and beyond. In: LPSC XXXV #1721 2004.
[33] Pearse RWB, Gaydon AG. The identification of molecular spectra. 4th ed. Chapman and Hall, John Wiley & Sons, Inc.; 1976.
[34] Huber KP, Herzberg G. Molecular spectra and molecular structure, IV. Constants of diatomic molecules. Van Nostrand Reinhold Company; 1979.
[35] Mihaly JM, Rosakis AJ, Adams MA, Tandy JD. Imaging ejecta and debris cloud behavior using laser side-lighting. In: Proceedings of the 12th hypervelocity impact symposium, procedia engineering 2012.
[36] Li B, Perotti L, Adams MA, Mihaly JM, Rosakis AJ, Stalzer M, et al. Large scale optimal transportation meshfree (OTM) simulations of hypervelocity impact. In: Proceedings of the 12th hypervelocity impact symposium, procedia engineering 2012.
[37] Adams M, Lashgari A, Li B, McKerns M, Mihaly J, Ortiz M, et al. Rigorous model based uncertainty quantification with application to terminal ballistics – part II. Systems with uncontrollable inputs and large scatter. J Mech Phys Solids 2011;60:1002–19.